Enhanced Thermoelectric Performance of *p*-type BiSbTe Through Incorporation of Magnetic CrSb

Raphael Fortulan[a,b,*], Suwei Li[c], Michael John Reece[c], Illia Serhiienko[d,e], Takao Mori[d,e], Sima Aminorroya Yamini[b,f,*]

[a]*Materials and Engineering Research Institute, Sheffield Hallam University, Sheffield, UK*
[b]*Present address: Unconventional Computing Laboratory, University of the West of England, Bristol, UK*
[c]*School of Engineering and Material Science, Queen Mary University of London, Mile End Road, London E1 4NS, UK*
[d]*International Center for Materials Nanoarchitectonics (WPI-MANA), National Institute for Materials Science, Tsukuba, Japan*
[e]*Graduate School of Pure and Applied Science, University of Tsukuba, Tsukuba, Japan*
[f]*School of Aerospace, Mechanical and Mechatronic Engineering, The University of Sydney, Sydney, 2006, Australia*

Abstract

This study investigates the thermoelectric properties of *p*-type $Bi_{0.5}Sb_{1.5}Te_3$ with added 10% Te composites containing a varying ratio of the ferromagnetic semiconductor of CrSb (0, 0.125, 0.5, and 1 wt.%) as a secondary phase. Samples were synthesized by a combination of ball milling and spark plasma sintering techniques. The incorporation of CrSb particles resulted in an increase in thermopower due to an increase in the effective mass of the charge carriers, indicating that there is a drag effect originating from the magnetic particles. However, this was at the expense of reduced electrical conductivity due to

*Corresponding authors
Email addresses: raphael.vicentefortulan@uwe.ac.uk (Raphael Fortulan), s.aminorroaya@uq.edu.au (Sima Aminorroya Yamini)

reduced carrier mobility. While overall only marginal improvements in power factors were observed, the multiphase samples exhibited significantly lower thermal conductivity compared to the single-phase material. As a result, a peak zT value of ~1.4 was achieved at 325 K for the sample with 0.125 wt.% CrSb. The synergistic effects of magnetically induced thermopower enhance- ment and thermal conductivity reduction resulted in showing the potential of incorporating magnetic secondary phases to optimize the thermoelectric performance in this system.

1. Introduction

Thermoelectric materials have been extensively studied as a green energy source due to their ability to directly convert thermal energy into electrical energy. The dimensionless figure of merit (zT) is defined as $zT = \alpha^2\sigma T/\kappa$, where α, σ, T, and κ are the thermopower, the electrical conductivity, the absolute temperature, and the thermal conductivity, respectively, is a metric that can be used to evaluate the performance of thermoelectric materials [1, 2].

To create a high-performance thermoelectric material, it is necessary to simultaneously achieve a high power factor ($PF = \alpha^2\sigma$) and a low total thermal conductivity (κ). However, α, σ, and κ exhibit strong correlations [3– 5], making the task of optimizing one parameter independently, while keeping the others constant, extremely challenging.

Bismuth telluride alloys are among the most efficient thermoelectric materials for near-room-temperature applications. Alloying Bi_2Te_3 with Sb_2Te_3 optimizes parameters such as carrier concentration, lattice thermal conduc-

tivity, and electronic band structure to improve the figure of merit zT [6, 7]. However, the thermoelectric performance of these alloys is limited by issues such as their relatively low thermopower.

Utilization of magnetism has emerged as a promising strategy to in- crease thermopower through mechanisms such as paramagnon drag and spin-dependent effects [8–11]. The concept that magnetism can possibly enhance thermoelectric properties dates back decades, with an early work proposing that magnon scattering could be the origin of an increase in the thermopower of some magnetic elements at low temperatures [Sorry, I think I missed writing this reference in the previous many corrections here that I made, it is: M. Bailyn: Phys. Rev., 126, 2040 (1962).]. The recent advancements include (1) using intrinsically magnetic semiconductors, such as MnTe [12], $CuFeS_2$ [13, 14], and $Cr_2Ge_2Te_6$ [15]; (2) doping non-magnetic thermoelectric materials with magnetic elements resulting in increased thermopower due to interactions between charge carriers and local magnetic moments [8, 16– 19]; and (3) introducing magnetic secondary phases, such as nanoparticles or inclusions, into non-magnetic thermoelectric matrices [20–23]. Studies on $Ba_{0.3}In_{0.3}Co_4Sb_{12}$ [20, 24] and $Ti_{0.25}Zr_{0.25}Hf_{0.5}NiSnSb$ [21] materials have shown that the inclusion of coherent magnetic particles can simultaneously enhance thermopower and carrier mobility. Magnetic secondary phases may allow the tuning of properties through the composition, size, and microstructure of the materials [25–29].

In this study, ball-milled stoichiometric $Bi_{0.5}Sb_{1.5}Te_3$ 10 at.% Te-rich and CrSb (0, 0.125, 0.5, and 1 wt.%) were fabricated by spark plasma sintering (SPS). Excess Te was added to the system as Te-rich bismuth telluride and bismuth antimony telluride alloys showed high thermoelectric performance

with a significant reduction in lattice thermal conductivity and suppression of

defects in the system [30–33]. The inclusion of excess Te suppresses the defects caused by its easy volatilization during the SPS process [34] and this strategy has been shown to result in more efficient thermoelectric materials [33]. CrSb is a ferromagnetic semiconductor with a Curie temperature of approximately 700 K [35], which makes it a promising magnetic secondary phase candidate for improving the thermoelectric performance of bismuth antimony telluride over a wide temperature range. By incorporating varying concentrations of magnetic CrSb particles, we were able to increase the thermopower through indicated drag effect, while maintaining a relatively high electrical conductivity. The addition of a secondary phase introduces additional phonon scattering mechanisms that reduce thermal conductivity. This, combined with the high thermopower, enabled a high peak of $zT \approx 1.4$ at 325 K.

2. Experimental details

2.1. Synthesis

A set of multiphase polycrystalline samples of $Bi_{0.5}Sb_{1.5}Te_{3+0.3}$ with x wt.% CrSb (x = 0, 0.125, 0.5, and 1) were synthesized by ball milling cast ingots of $Bi_{0.5}Sb_{1.5}Te_{3+0.3}$ and CrSb. First, $Bi_{0.5}Sb_{1.5}Te_{3+0.3}$ samples were synthesized by direct reaction of stoichiometric amounts of high purity elements of Bi shots (99.999%, Alfa Aesar), Te pieces (99.999%, Alfa Aesar), and Sb shots (99.999%, Alfa Aesar) in vacuum-sealed quartz ampules loaded in an inert atmosphere glove box. The ampule was heated to 850 °C for 12 h, homogenized at 1000 °C, quenched in cold water, and then annealed at 400 °C for 72 h. Second, a pristine CrSb sample was also synthesized by loading stoichiometric amounts of Cr 60 mesh powder (99.95%, Alfa Aesar) and Sb shots (99.999%,

Alfa Aesar) into a vacuum-sealed quartz ampule. The ampule was heated to 850 °C for 24 h, mixed every 4 h, homogenized at 1160 °C for 1 h, and allowed to cool naturally in a furnace. The resulting ingot was hand-ground using an agate mortar and pestle housed inside a glove box, loaded into a vacuum-sealed quartz tube, and annealed at 900 °C for 24 hours to eliminate the presence of a $CrSb_2$ impurity phase. The annealed powder was then loaded into a graphite die and sintered under vacuum to produce 11-mm-diameter rods by SPS (KCE FCT-H HP D-25 SD, FCT Systeme GmbH, Rauenstein, Germany) at a pressure of 50 MPa for 20 min at 1173 K. The density of the sample was 99.9% of its nominal value. In sequence, the cast ingots were manually pre-milled using an agate mortar and pestle housed inside a glovebox. The powders were weighed and placed in a 250 mL agate jar along with 20 mm agate balls and absolute ethanol (99.97%, VWR). The ball-to-powder ratio was 15:1, and the solvent-to-powder ratio used was 100 ml to 10 g [36]. The milling process was conducted using a Retsch Planetary Ball Mill PM 100 at 300 rpm for 4 h at 15 min intervals with a 5 min break and a change in direction halfway through the milling process. The jar was then placed in a desiccator for at least 15 h. The dried powders were then placed into a graphite die and sintered under vacuum to fabricate 11 mm diameter rods using SPS. The samples were sintered at 50 MPa for 5 min at 400 °C. The densities of all the samples were measured based on the rod dimensions and weight. The average density of the samples was approximately 95% of their nominal density.

3. Materials characterization

The phase purity and crystal structure of the sintered samples were characterized by Powder X-ray Diffraction (PXRD) using a PANalytical X'Pert Pro diffractometer with CuKα1 radiation (λ = 0.154 06 nm, 40 kV, 40 mA). Electrical conductivity (σ) and thermopower (α) were measured perpendicular to the sintering direction of the samples by cutting $\approx 2 \times 2 \times 8$ mm^3 bar specimens from the rods. Measurements were conducted from room temperature to 523 K under helium atmosphere using a Linseis LSR-3 apparatus. The thermal diffusivity (D) of all the samples was measured by the LFA method using a NETZSCH LFA 467 HyperFlash® instrument. Slab-shaped samples were also cut to measure the room-temperature Hall coefficient (R_H) under a ±0.55 T magnetic field using an ECOPIA 3000 Hall Effect Measurement System. The Hall carrier concentration (n_H) was calculated as $n_H = 1/(e \cdot R_H)$.

Heat capacity measurements were conducted from room temperature to 473 K using a PerkinElmer DSC 8000 according to the ASTM sapphire standard method E1269 and from 473 K to 773 K using a TA Instruments SDT 650 simultaneous thermal analyzer according to the ASTM modulated DSC method E2716. The measured heat capacity values are shown in the Supporting Information.

4. Results and discussion

4.1. Structural and phase analysis

The phase purity and crystal structure of all samples were determined by indexing their PXRD patterns, as shown in figure 1. All samples matched

a single-phase rhombohedral $Bi_{0.5}Sb_{1.5}Te_3$ phase, with no impurity phases detected. It should be noted that the typical detection range for XRD phase analysis is 5 ~10% [37]. Therefore, given the low concentrations of this set of samples, it was expected that no CrSb peaks would be detected. The phase

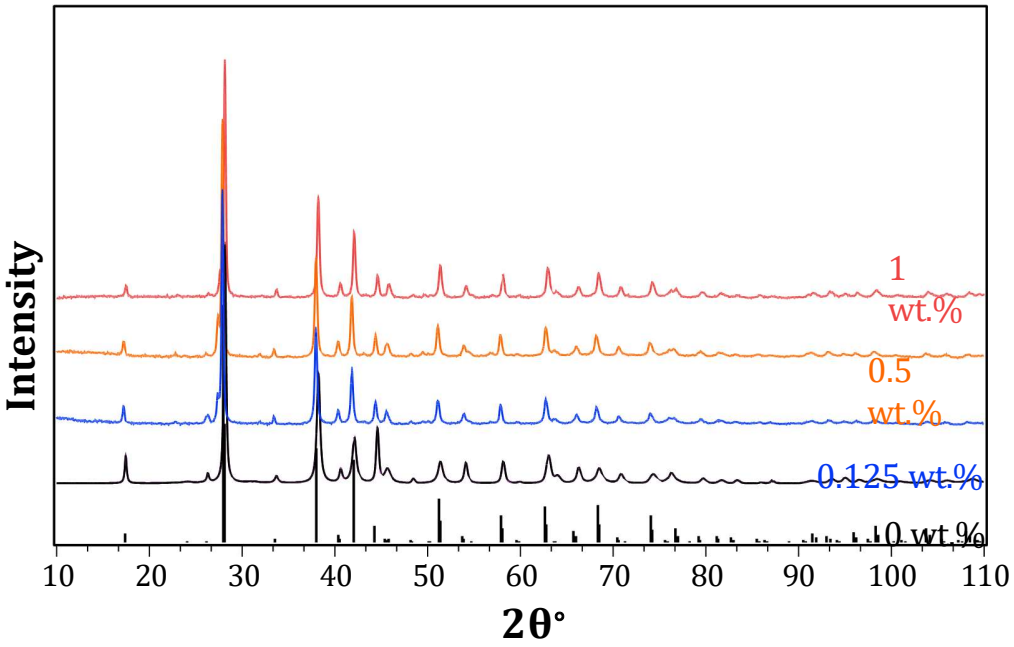

Figure 1: Powder X-ray diffraction patterns of $Bi_{0.5}Sb_{1.5}Te_{3+0.3}$ with x wt.% CrSb (x = 0, 0.125, 0.5, and 1) samples.

purity and crystal structure of the CrSb sample were determined by indexing its PXRD pattern (see fig. S2 in the Supporting Information).

4.2. Transport properties

Figure 2 shows the thermopower, electrical conductivity, and power factor of $Bi_{0.5}Sb_{1.5}Te_{3+0.3}$ with x wt.% CrSb (x = 0, 0.125, 0.5, and 1), measured perpendicular to the direction of sintering. All samples showed a positive

thermopower (fig. 2(a)), indicating a *p*-type semiconductor behavior. The electrical conductivity exhibited metallic behavior with decreasing values, as shown in figure 2(b).

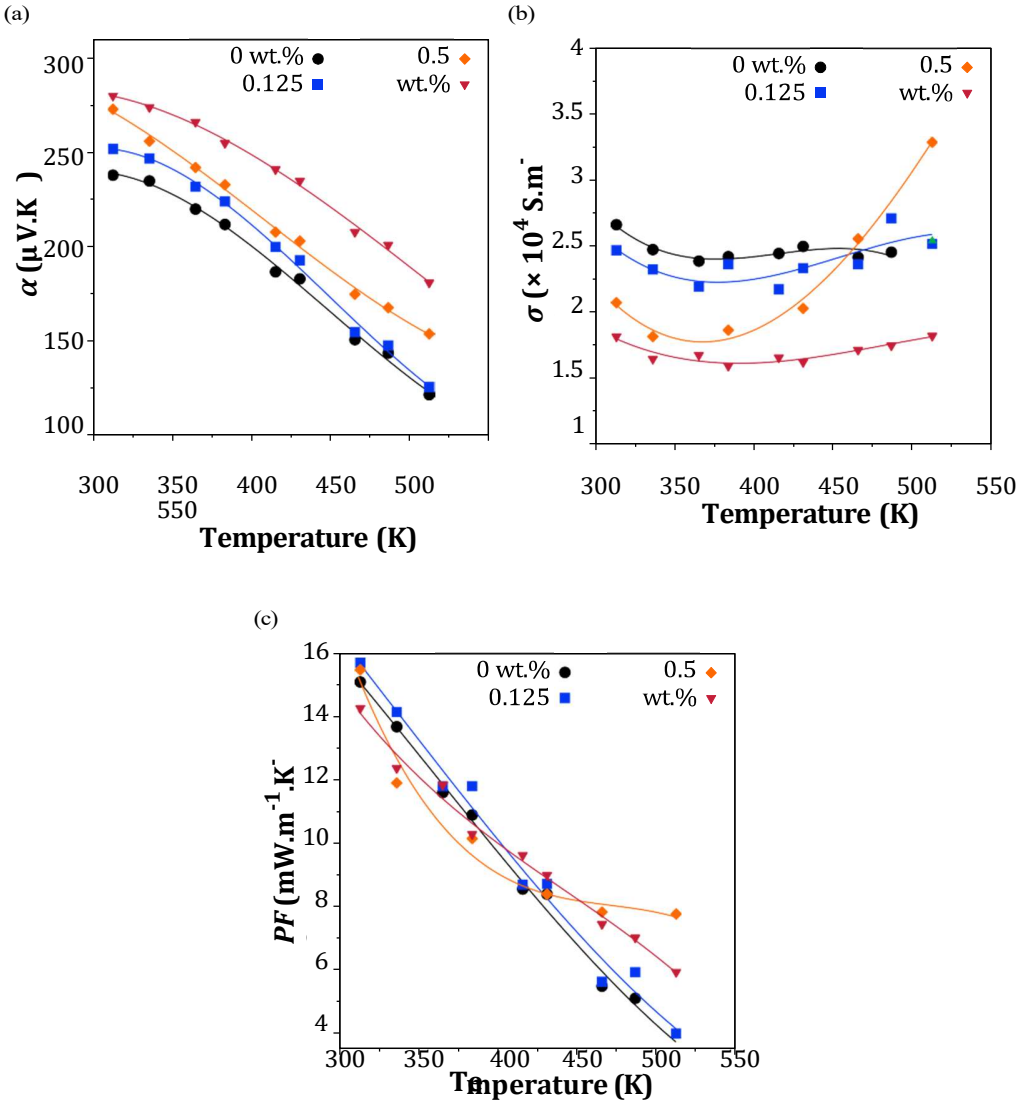

Figure 2: Temperature dependence of the (a) thermopower, (b) electrical conductivity, and (c) power factor of ball milled $Bi_{0.5}Sb_{1.5}Te_{3+0.3}$ with *x* wt.% CrSb (*x* = 0, 0.125, 0.5, and 1) samples.

The room-temperature values of the thermopower increase with the addition of the second phase, rising from ~238 $\mu V.K^{-1}$ for the single-phase sample and from ~215 $\mu V.K^{-1}$ to ~270 $\mu V.K^{-1}$ for the 1 wt.% CrSb. With the opposite effect on electrical conductivity, the electrical conductivity of the single-phase sample decreased from ~2.7×10^4 $S.m^{-1}$ to ~1.8×10^4 $S.m^{-1}$.

Table 1 lists the Hall carrier concentrations and mobilities of the samples. The carrier concentrations are lower than those observed in the literature (e.g. ~1×10^{19} cm^{-3} [33]) which the overall lower electrical conductivity of the samples. The mobility values of 232 $cm^2.V^{-1}.s^{-1}$ of the single-phase samples are similar to those reported in the literature (e.g., 248 $cm^2.V^{-1}.s^{-1}$ [30]). The values of n_H ranged from 7.7 ~ 7.1 10^{18} cm^{-3}, indicating that the addition of Te to the system stabilized the carrier concentration of the samples. However, the mobility decreases with the inclusion of the secondary phase, which is consistent with the behavior of multiphase materials [38, 39].

Table 1: Hall carrier concentration and mobility of ball milled $Bi_{0.5}Sb_{1.5}Te_{3+0.3}$ with x wt.% CrSb (x = 0, 0.125, 0.5, and 1) samples

x	n_H(× 10^{18} cm^{-3})	μ_H ($cm^2.V^{-1}.s^{-1}$)
0	7.7	232.0
0.125	7.7	203.9
0.5	7.3	185.5
1	7.1	161.6

The thermopower of the CrSb-added samples increased overall with the inclusion of the secondary phase. Since the carrier concentration of all samples

has similar values, these changes cannot simply be attributed to changes in the values of n_H. The behavior of the band structure with CrSb inclusion was analyzed by modeling the thermopower and Hall carrier concentration using the single parabolic band (SPB) model [40] (see Supporting Information for more details). The SPB model used here may not fully and accurately determine the behavior of multiphase samples due to the presence of bipolar conduction, complex scattering processes, and the non-parabolic nature of the valence band. However, this approach can indicate a trend in the calculated effective mass m^* of samples [41]. The calculated effective masses for all the samples are listed in table 2. The effective mass of the samples increased

Table 2: Calculated effective mass of ball milled $Bi_{0.5}Sb_{1.5}Te_{3+0.3}$ with x wt.% CrSb (x = 0, 0.125, 0.5, and 1) samples using the single parabolic band model

x	m^*/m_0
0	0.90
0.125	1.16
0.5	1.06
1	1.21

in the presence of the secondary phase, in alignment with the trend of the thermopower. This trend is visible in both table 2 and in the dependence between the thermopower α, carrier concentration n, and m^* shown in the Pisarenko plot in figure 3. The thermopower for a degenerate semiconductor, with a parabolic band and energy-independent scattering approximation, can

be written as [40]

$$\alpha = \frac{8\pi^2 k_B}{3qh^2} m^* T \left(\frac{\pi}{3n}\right)^{2/3}, \quad (1)$$

where m^* is the effective mass of the DOS.

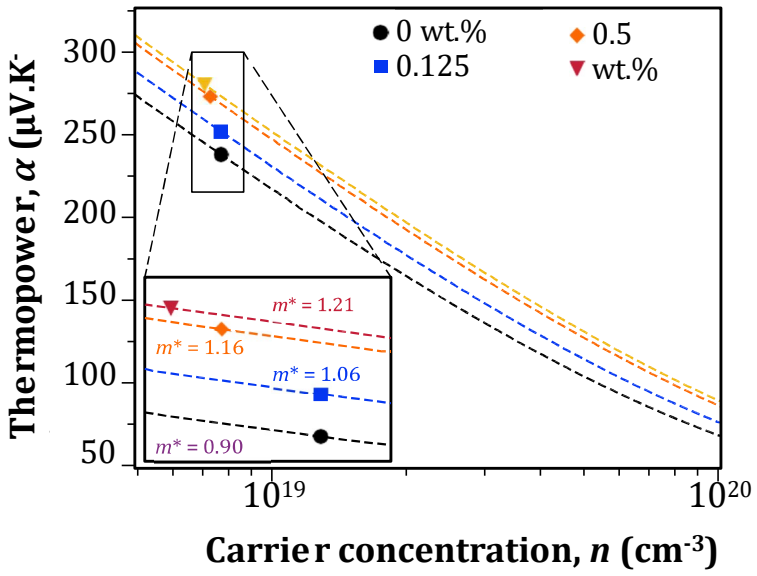

Figure 3: The Pisarenko plots (thermopower versus Hall carrier concentration) at room temperature for ball milled $Bi_{0.5}Sb_{1.5}Te_{3+0.3}$ with x wt.% CrSb (x = 0, 0.125, 0.5, and 1). The dashed lines represent the calculated values from the SPB model using the effective masses as shown in the inset.

Equation 1 shows a direct proportionality between the thermopower and effective mass. This suggests that the presence of a magnetic phase in the material can lead to an increase in the effective mass of the sample and consequently an increase in the thermopower, similar to observations of studies with magnetic dopants [16, 42]. Interestingly, the results show that despite the presence of a magnetic secondary phase with poor thermoelectric performance and low thermoelectric power of approximately 12.5 $\mu V.K^{-1}$ at

room temperature and 4.38 $\mu V.K^{-1}$ at 545 K, the electrical performance of the samples can be improved rather than degraded (see Supporting Information for CrSb data). However, the combined decrease in carrier mobility due to the presence of an additional phase and the possible dragging effect caused by the magnetic phase severely degrades the electrical conductivity of multiphase samples [16]. Consequently, there was only a marginal increase in the power factor PF (as shown in fig. 2(c)).

The thermal conductivity (κ) of the samples is shown in figure 4(a). As the temperature increased, the thermal conductivity (κ) of all samples started to increase. The electronic contribution to the thermal conductivity (κ_e) is shown in figure 4(b) and it was estimated using the Wiedemann-Franz law [43] ($\kappa_e = L\sigma T$) where L is the Lorenz number, and it was calculated using the SPB model (see Supporting Information for more details).

Since multiphase samples have lower electrical conductivity, κ_e is reduced accordingly. The lattice (κ_l) contributions to thermal conductivity were calculated as $\kappa_l = \kappa - \kappa_e$, as shown in figure 4(c). All samples exhibited optimized behavior when compared to the single-phase sample.

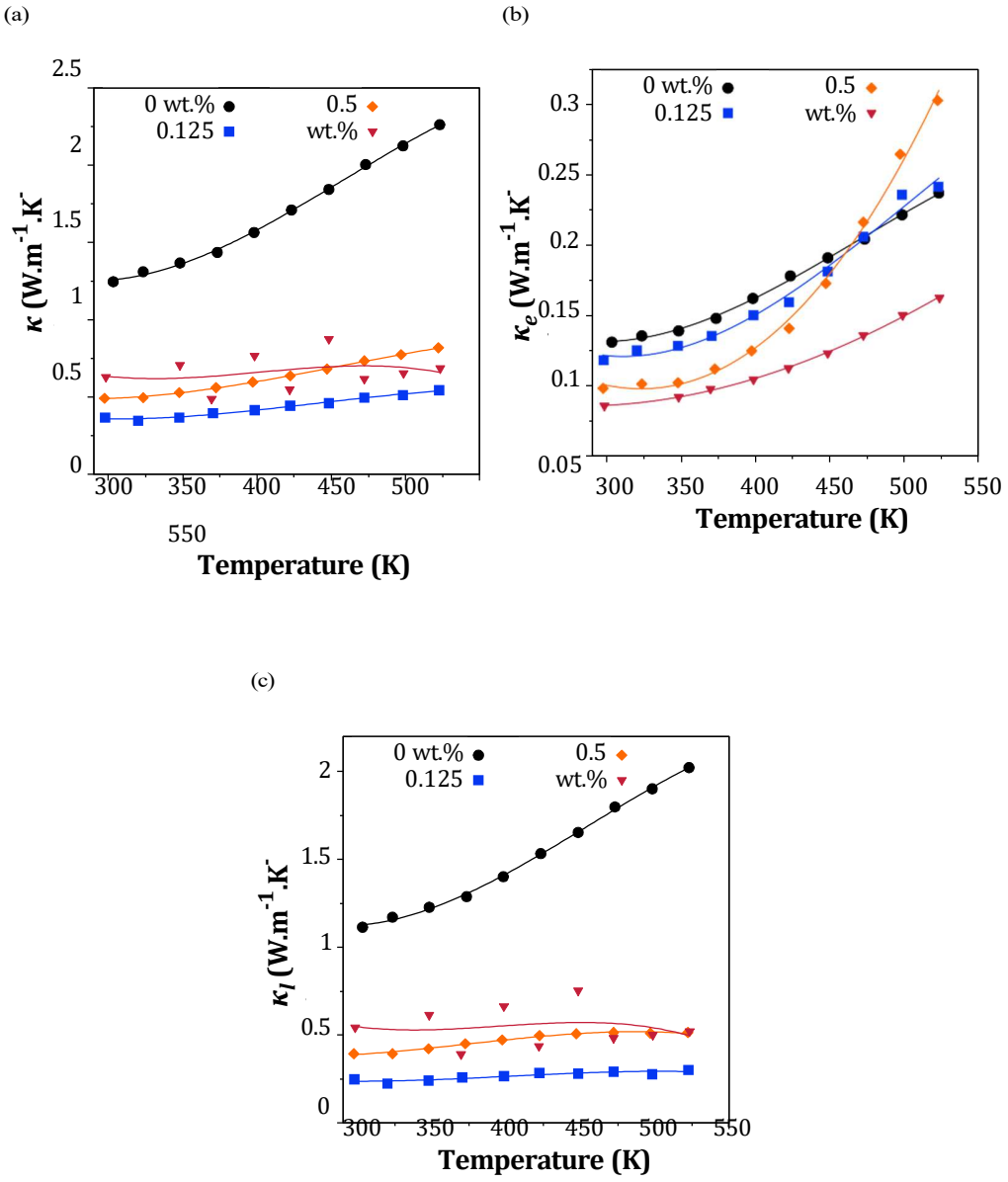

Figure 4: Temperature dependence of the (a) thermal conductivity, (b) electronic thermal conductivity, and (c) lattice thermal conductivity of $Bi_{0.5}Sb_{1.5}Te_{3+0.3}$ with *x* wt.% CrSb (*x* = 0, 0.125, 0.5, and 1) samples.

The figure of merit (zT) of the samples is shown in Figure 5. The combination of significantly reduced thermal conductivity, aligned with an increase in thermal power due to the incorporation of the magnetic secondary phase, contributed to the high zT values for the multiphase samples compared to the single-phase $Bi_{0.5}Sb_{1.5}Te_{3+0.3}$ material. The 0.125 wt.% CrSb sample exhibited the highest zT, reaching a peak value of ~1.4 at 325 K. This represents a remarkable ~400% improvement over the pristine sample, which only achieved $zT \approx 0.35$ at the same temperature. The other multiphase compositions also showed promising zT improvements, albeit to a lesser extent. The 0.5 wt.% CrSb had the next highest zT of ~0.92 at 525 K, followed by the 1 wt.% at ~0.68. This trend suggests that similar to doping, there is likely to be an optimum doping level beyond which the benefits diminish due to the excessive degradation of the electrical properties. The high zT values result from the synergistic effects of magnetically induced thermopower enhancement and thermal conductivity reduction due to interfacial scattering in the multiphase samples. These results suggest that the incorporation of magnetic phases may be an effective strategy to optimize the thermoelectric performance of bulk materials such as $Bi_{0.5}Sb_{1.5}Te_{3+0.3}$.

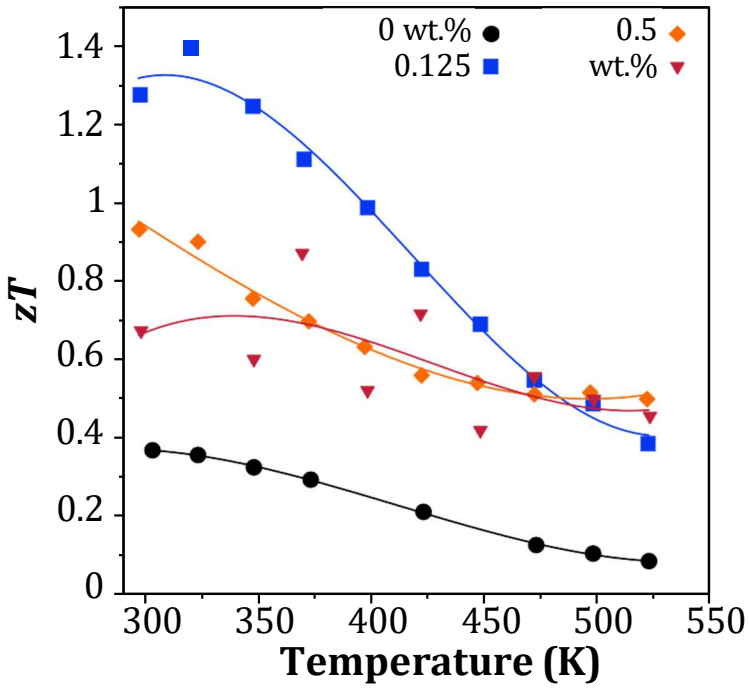

Figure 5: Temperature dependence of zT of $Bi_{0.5}Sb_{1.5}Te_{3+0.3}$ with x wt.% CrSb (x = 0, 0.125, 0.5, and 1) samples.

5. Conclusions

In this study, a series of multiphase $Bi_{0.5}Sb_{1.5}Te_{3+0.3}$ samples with varying concentrations of CrSb magnetic secondary phase (0, 0.125, 0.5, and 1 wt. %) were successfully synthesized by a combination of ball milling and spark plasma sintering techniques. The results showed that the incorporation of small amounts of the CrSb magnetic phase significantly enhanced the thermopower of the samples by increasing the carriers' effective mass, which is consistent with previous findings for magnetic dopants. However, the electrical

conductivity is adversely affected by the reduced carrier mobility caused by the presence of the secondary phase. As a result, only marginal improvements in power factor were observed. Despite the limited power factor improvement, the multiphase samples exhibited significantly lower thermal conductivity than the single-phase material. This effect, combined with the increased power factors, resulted in a relatively high figure of merit (zT) values for multiphase compounds, particularly at around room temperature. These results confirm the potential benefits of incorporating magnetic secondary phases into thermoelectric materials to modulate their electronic and thermal transport properties favorably.

Acknowledgements

This study was supported by the European Union's Horizon 2020 research and innovation program under the Marie Sklodowska-Curie Grant Agreement No. 801604. This work also received support from the Henry Royce Institute for Advanced Materials, funded through EPSRC grants EP/R00661X/1, EP/S019367/1, EP/P025021/1, and EP/P025498/1. TM would like to thank JST Mirai Program Grant Number JPMJMI19A1. IS was also supported by JST SPRING, Grant Number JPMJSP2124.

References

1. Tang, Y. *et al.* Convergence of Multi-Valley Bands as the Electronic Origin of High Thermoelectric Performance in CoSb3 Skutterudites. *Nature Materials* **14,** 1223–1228. issn: 1476-4660. (2024) (Dec. 2015).
2. Wu, Y. *et al.* Lattice Strain Advances Thermoelectrics. *Joule* **3,** 1276–1288 (2019).
3. Zhang, M. *et al.* Identifying the Manipulation of Individual Atomic-Scale Defects for Boosting Thermoelectric Performances in Artificially Controlled Bi2Te3 Films. *ACS Nano* **15,** 5706–5714. issn: 1936-0851. (2024) (Mar. 2021).
4. Yang, G. *et al.* Ultra-High Thermoelectric Performance in Bulk BiSbTe/Amorphous Boron Composites with Nano-Defect Architectures. *Advanced Energy Materials* **10,** 2000757. issn: 1614-6840. (2024) (2020).
5. Hendricks, T., Caillat, T. & Mori, T. Keynote Review of Latest Advances in Thermoelectric Generation Materials, Devices, and Technologies 2022. *Energies* **15,** 7307. issn: 1996-1073. https://www.mdpi.com/1996-1073/15/19/7307 (2024) (19 Jan. 2022).
6. Witting, I. T. *et al.* The Thermoelectric Properties of Bismuth Telluride. *Adv. Electron. Mater.* **5** (2019).
7. Witting, I. T., Ricci, F., Chasapis, T. C., Hautier, G. & Snyder, G. J. The Thermoelectric Properties of n -Type Bismuth Telluride: Bismuth Selenide Alloys Bi2Te3-xSex. *Research* **2020,** 1–15 (Mar. 31, 2020).

8. Ahmed, F., Tsujii, N. & Mori, T. Thermoelectric Properties of CuGa1-xMnxTe2: Power Factor Enhancement by Incorporation of Magnetic Ions. *J. Mater. Chem.A* **5,** 7545–7554 (Apr. 18, 2017).

9. Koshibae, W., Tsutsui, K. & Maekawa, S. Thermopower in Cobalt Oxides. *Physical Review B* **62,** 6869–6872. https://link.aps.org/doi/10.1103/PhysRevB.62.6869 (2024) (Sept. 15, 2000).

10. Tsujii, N., Nishide, A., Hayakawa, J. & Mori, T. Observation of Enhanced Thermopower Due to Spin Fluctuation in Weak Itinerant Ferromagnet. *Sci. Adv.* **5,** eaat5935.

11. Zheng, Y. *et al.* Paramagnon Drag in High Thermoelectric Figure of Merit Li-doped MnTe. *Science Advances* **5,** eaat9461. https://www.science.org/doi/10.1126/sciadv.aat9461 (2024) (Sept. 13, 2019).

12. Wasscher, J. D. & Haas, C. Contribution of Magnon-Drag to the Thermoelectric Power of Antiferromagnetic Mn Te. *Phys. Lett. B* **8,** 302–304 (Mar. 1, 1964).

13. Tsujii, N. & Mori, T. High Thermoelectric Power Factor in a Carrier-Doped Magnetic Semiconductor CuFeS2. *Appl. Phys. Express* **6,** 043001 (Apr. 2013).

14. Ang, R. *et al.* Thermoelectricity Generation and Electron-Magnon Scattering in a Natural Chalcopyrite Mineral from a Deep-Sea Hydrothermal Vent. *Angew. Chem. Int. Ed. Engl.* **54,** 12909–13. PMID: 26332260 (Oct. 26, 2015).

15. Peng, C. *et al.* Improvement of Thermoelectricity Through Magnetic Interactions in Layered Cr2Ge2Te6. *physica status solidi (RRL) - Rapid Research Letters* **12,** 1800172 (2018).

16. Vaney, J. B. *et al.* Magnetism-Mediated Thermoelectric Performance of the Cr-Doped Bismuth Telluride Tetradymite. *Mater. Today Phys.* **9,** 100090 (June 2019).

17. Acharya, S., Anwar, S., Mori, T. & Soni, A. Coupling of Charge Carriers with Magnetic Entropy for Power Factor Enhancement in Mn Doped Sn1.03Te for Thermoelectric Applications. *J. Mater. Chem. C* **6,** 6489–6493 (June 21, 2018).

18. Das, S., Valiyaveettil, S. M., Chen, K.-H., Suwas, S. & Mallik, R. C. Thermoelectric Properties of Mn Doped BiCuSeO. *Mater. Res. Express* **6** (2019).

19. Matsuura, H., Ogata, M., Mori, T. & Bauer, E. Theory of Huge Thermoelectric Effect Based on a Magnon Drag Mechanism: Application to Thin-Film Heusler Alloy. *Physical Review B* **104,** 214421. `https://link.aps.org/doi/10.1103/PhysRevB.104.214421` (2024) (Dec. 15, 2021).

20. Zhao, W. *et al.* Magnetoelectric Interaction and Transport Behaviours in Magnetic Nanocomposite Thermoelectric Materials. *Nat. Nanotechnol.* **12,** 55–60. PMID: `27723733` (Jan. 2017).

21. Lu, R. *et al.* Coherent Magnetic Nanoinclusions Induce Charge Localization in Half-Heusler Alloys Leading to High-Tc Ferromagnetism and

Enhanced Thermoelectric Performance. *J. Mater. Chem.A* **7,** 11095–11103 (May 7, 2019).

22. Liu, K. G. & Li, J. Thermoelectric Properties of Bulk FeSb2 and the Composite of FeSb2 and CoSb3 Prepared by Sintering. *Frontiers of Green Building, Materials and Civil Engineering, Pts 1-8* **71–78,** 3741–3744 (2011).

23. Bourgès, C. *et al.* Investigation of Mn Single and Co-Doping in Thermoelectric CoSb3-Skutterudite: A Way Toward a Beneficial Composite Effect. *ACS Applied Energy Materials* **6,** 9646–9656. https://doi.org/10.1021/acsaem.3c01725 (2024) (Sept. 25, 2023).

24. Gao, Y.-H., Chen, H., Liu, N. & Zhang, R.-Z. Criteria for Power Factor Improvement in Thermoelectric Composite. *Results Phys.* **11,** 915–919 (Dec. 1, 2018).

25. Liu, Z. *et al.* Candidate for Magnetic Doping Agent and High-Temperature Thermoelectric Performance Enhancer: Hard Magnetic M-Type BaFe12O19 Nanometer Suspension. *ACS Appl. Mater. Interfaces* **11,** 45875–45884 (Dec. 11, 2019).

26. Marghussian, V. in *Nano-Glass Ceramics* 181–223 (Elsevier, 2015). isbn: 978-0-323-35386-1.

27. Tan, G. *et al.* Valence Band Modification and High Thermoelectric Performance in SnTe Heavily Alloyed with MnTe. *J. Am. Chem. Soc.* **137,** 11507–16. PMID: 26308902 (Sept. 9, 2015).

28. Vandendriessche, S., Brullot, W., Slavov, D., Valev, V. K. & Verbiest, T. Magneto-Optical Harmonic Susceptometry of Superparamagnetic Materials. *Appl. Phys. Lett.* **102,** 161903 (Apr. 22, 2013).

29. Zhao, W. *et al.* Superparamagnetic Enhancement of Thermoelectric Performance. *Nature* **549,** 247–251. PMID: 28905895 (Sept. 13, 2017).

30. Zhuang, H.-L. *et al.* Thermoelectric Performance Enhancement in BiSbTe Alloy by Microstructure Modulation via Cyclic Spark Plasma Sintering with Liquid Phase. *Advanced Functional Materials* **31,** 2009681 (2021).

31. Liu, Y. *et al.* Crystallographically Textured Nanomaterials Produced from the Liquid Phase Sintering of BixSb2-xTe3 Nanocrystal Building Blocks. *Nano Letters* **18,** 2557–2563 (Mar. 2018).

32. Deng, R. *et al.* Thermal Conductivity in Bi0.5Sb1.5Te3+x and the Role of Dense Dislocation Arrays at Grain Boundaries. *Science Advances* **4,** eaar5606 (June 2018).

33. Chauhan, N. S. *et al.* Compositional Fluctuations Mediated by Excess Tellurium in Bismuth Antimony Telluride Nanocomposites Yield High Thermoelectric Performance. *The Journal of Physical Chemistry C* **125,** 20184–20194 (Sept. 23, 2021).

34. Kim, H.-S. *et al.* High Thermoelectric Performance in (Bi0.25Sb0.75)2Te3 Due to Band Convergence and Improved by Carrier Concentration Control. *Mater. Today* **20,** 452–459 (Oct. 1, 2017).

35. Franzen, H. & Sterner, C. The X-Ray Photoelectron Spectra of MnS, MnSe, and MnTe. *J. Solid State Chem.* **25,** 227–230 (July 1, 1978).

36. Kanatzia, A., Papageorgiou, C., Lioutas, C. & Kyratsi, T. Design of Ball-Milling Experiments on Bi2Te3 Thermoelectric Material. *Journal of Electronic Materials* **42,** 1652–1660 (Dec. 2012).

37. Holder, C. F. & Schaak, R. E. Tutorial on Powder X-ray Diffraction for Characterizing Nanoscale Materials. *ACS Nano* **13,** 7359–7365 (July 2019).

38. Ko, D. K., Kang, Y. & Murray, C. B. Enhanced Thermopower via Carrier Energy Filtering in Solution-Processable Pt-Sb2Te3 Nanocomposites. *Nano Lett.* **11,** 2841–4. PMID: 21630679 (July 13, 2011).

39. Zhang, Y.-X., Zhu, Y.-K., Song, D.-S., Feng, J. & Ge, Z.-H. Excellent thermoelectric performance achieved in Bi2Te3/Bi2S3Bi nanocomposites. *Chemical Communications* **57,** 2555–2558 (2021).

40. Snyder, G. J. & Toberer, E. S. Complex Thermoelectric Materials. *Nature Materials* **7,** 105–114 (Feb. 2008).

41. Zheng, Y. *et al.* Mechanically Robust BiSbTe Alloys with Superior Thermoelectric Performance: A Case Study of Stable Hierarchical Nanostructured Thermoelectric Materials. *Advanced Energy Materials* **5,** 1401391 (2015).

42. Fortulan, R. *et al.* Thermoelectric Performance of n-Type Magnetic Element Doped Bi2S3. *ACS Applied Energy Materials* **5,** 3845–3853 (Mar. 2022).

43. Jonson, M. & Mahan, G. D. Mott's Formula for the Thermopower and the Wiedemann-Franz Law. *Phys. Rev. B* **21,** 4223–4229 (1980).